# Wave field simulation on 3D borehole dipole radiation

Junxiao Li, Kris Innanen, Kuo Zhang, Guo Tao and Laurence R. Lines

## ABSTRACT

Wave simulation in borehole environment is crucial for characterization of the waveforms traveling through the borehole, recorded by the receivers, leaking away outside bore hole and reflecting from geological structures outside borehole. One of the flaws of the omni-directional monopole acoustic prototype is it only measures the acoustic pressure and is therefore insensitive to determine the reflector azimuth. In order to mitigate this directional ambiguity, a dipole acoustic reflection imaging is developed. In this paper, a 3D elastic staggered-grid finite difference method for both isotropic and anisotropic media is discussed for the borehole acoustic wave simulation. Based on the convolutional perfectly matched layer and the multi-axial perfectly matched layer scheme, a hybrid perfectly matched layer is proposed which removes the artificial reflections from the computational regions. A numerical simulation of radiation, reflection and multipole reception of the elastic waves in the presence of a dipole source is proposed, for azimuthal detection, to characterize the relationship between S wave polarization and the offset between the source and receivers as well as the angle of the source and reflector. The results show the amplitude change of S-S reflection is related to the incident angle to the reflector. Its maximum amplitude occurs as the incident angle reaches to a critical angle, which can then be used to calculate the total propagation distance of the S-S wave. As a result, the critical angle as well as the SH wave velocity of the second layer outside the borehole can thus be determined.

## INTRODUCTION

Acoustic reflection imaging logging, dating back to 1989 when Hornby (1989) presented data processing and imaging methods for sonic tool BARS (borehole acoustic reflection survey) developed by Schlumberger, uses the leaky energy as incident waves, and probes reflections from near bore hole fractures and micro-structures. By analyzing received waveform signals, we can obtain structural information concerning nearby formations and evaluate small subtle and fractured reservoirs. In further research involving acoustic reflection imaging, monopole acoustic imaging has produced positive results in delineating near borehole structures (Fortin et al., 1991; Coates et al., 2000; Li et al., 2002). One of the flaws of the omni-directional monopole acoustic prototype however, is it only measures the acoustic pressure without determining the reflector azimuth. In order to mitigate this directional ambiguity, dipole acoustic reflection imaging is developed (Tang et al., 2003; Tang, 2004; Tang and Patterson, 2009; Bolshakov et al., 2011). In dipole methods, dispersive flexure waves, whose velocity at the cutoff frequency equals the S-wave velocity, are analyzed. These data, given the deviation angle of the well bore and the tool azimuthal angle, can determine the azimuth of the structures outside the borehole after migration (Tang et al., 2003).

Key to this technology is accurate elastic wave simulation. For wavefield simulation in fluid-filled borehole environments, the finite difference (FD) method is widely used.

The staggered-grid FD was first proposed by Madariaga (1976), and further developed by Virieux (1986) who focused on the P-SV wave case by using staggered-grid FD method and Berenger (1994) proposed a fourth-order staggered-grid FD method. Because the staggered-grid schemes have advantages over non-staggered grid ones, such as competence in the presence of liquid-solid interfaces, it has gained popularity in seismic wave modeling and bore hole acoustic well logging modeling. One of the issues that the FD method has to face is how to effectively mitigate artificial reflections from the computation boundaries. During last decades, scholars have proposed a variety of methods for this purpose, such as sponge zones (Cerjan et al., 1985; Sochacki et al., 1987), optimized conditions (Peng and Toksöz, 1995), the eigenvalue decomposition method (Dong et al., 2005), continued fraction absorbing conditions (Guddati and Lim, 2006), exacting absorbing conditions on a spherical contour (Grote, 2000), or asymptotic local or nonlocal operators (Givoli, 1991; Hagstrom and Hariharan, 1998). No complete solution to the problem of boundary reflections at grazing incidence is yet available, however. Furthermore, all of these methods introduce significant computational expense into the processing flow. So, a need remains to develop efficient high fidelity simulation tools for the borehole dipole imaging problem.

In this paper, we discuss use of the 3D staggered-grid FD method as a tool for borehole acoustic well logging. The perfectly matched layer (Berenger, 1994), the convolutional perfectly matched layer (Kuzuoglu and Mittra, 1996) and the multiaxial perfectly matched layer (Meza-Fajardo and Papageorgiou, 2008) are then introduced and discussed as methods to suppress artificial reflections. Based on the convolutional perfectly matched layer and the multiaxial perfectly matched layer scheme, a hybrid perfectly matched layer is proposed in this paper. A numerical simulation of radiation, reflection and multipole reception of the elastic waves for a dipole source is proposed to permit azimuthal detection for a dipole source, and the relationship between S wave polarization and the offset between the source and receivers as well as the angle of the source and reflector.

## THEORY AND PRINCIPLES

### Finite difference method

As one of the most widely used methods, finite difference method in its early applications was mainly based on the displacement formulation of wave equation (Alterman and Karal, 1968; Kelly et al., 1976), in which the second order wave equations are discretized on grids, that is, the computational domain is covered by a space-time grid.

After the first proposal of the staggered grid scheme (Madariaga, 1976), it gained an increasing number of scholars' favor to apply in wave field simulation (Virieux, 1986; Levander, 1988). Yoon and McMechan (1992) applied the 3D finite difference forward simulations for wave propagation in borehole environments. Wave propagation in an elastic medium can be expressed by equation of motion as:

$$\rho \partial_i^2 u_i = \sigma_{ij,j} \tag{1}$$

where $\rho$ is density, $u_i$ is the displacement vector and $\sigma_{ij}$ is stress tensor, $\sigma_{ij,j}$ means the spatial derivatives of stress tensor. The summation convention for repeated subscripts is also applied. According to Hook's law, the relationship between stress and strain tensor

can be described as,

$$\sigma_{ij,j} = c_{ijkl}\varepsilon_{kl} \tag{2}$$

where $c_{ijkl}$ are the elastic constants, and the strain tensor $\varepsilon_{kl}$ is defined as,

$$\varepsilon_{kl} = \frac{1}{2}(u_{k,l} + u_{l,k}) \tag{3}$$

In isotropic medium, the elastic constant tensor can be described as,

$$c_{ijkl} = \lambda\delta_{ij}\delta_{kl} + \mu(\delta_{ik}\delta_{jl} + \delta_{il}\delta_{jk}) \tag{4}$$

where, $\delta_{ij}$ is the Kronecker delta, which equals to 1 when $i = j$, otherwise equals to zero. $\lambda$ and $\mu$ are the Lamé constants, by which, the P and S wave velocity $\alpha$ and $\beta$ are given as $\sqrt{(\lambda + 2\mu)/\rho}$ and $\sqrt{\mu/\rho}$. And the stress tensor in equation (2) can be described as,

$$\sigma_{ij} = \lambda(\nabla \cdot u)\delta_{ij} + 2\mu\varepsilon_{ij} \tag{5}$$

The matrix form of equation (2) can be described as,

$$\begin{bmatrix}\sigma_{11}\\ \sigma_{22}\\ \sigma_{33}\\ \sigma_{23}\\ \sigma_{23}\\ \sigma_{12}\end{bmatrix} = \begin{bmatrix}c_{11} & c_{12} & c_{13} & c_{14} & c_{15} & c_{16}\\ c_{21} & c_{22} & c_{23} & c_{24} & c_{25} & c_{26}\\ c_{31} & c_{32} & c_{33} & c_{34} & c_{35} & c_{36}\\ c_{41} & c_{42} & c_{43} & c_{44} & c_{45} & c_{46}\\ c_{51} & c_{52} & c_{53} & c_{54} & c_{55} & c_{16}\\ c_{61} & c_{62} & c_{63} & c_{64} & c_{65} & c_{66}\end{bmatrix} \begin{bmatrix}\varepsilon_{11}\\ \varepsilon_{22}\\ \varepsilon_{33}\\ 2\varepsilon_{23}\\ 2\varepsilon_{13}\\ 2\varepsilon_{12}\end{bmatrix} \tag{6}$$

In the above equation, the elastic constant tensor in a vertical transverse isotropic medium (VTI) can be described as,

$$c_{VTI} = \begin{bmatrix} c_{11} & c_{11}-2c_{66} & c_{13} & 0 & 0 & 0\\ c_{11}-2c_{66} & c_{11} & c_{13} & 0 & 0 & 0\\ c_{13} & c_{13} & c_{33} & 0 & 0 & 0\\ 0 & 0 & 0 & c_{44} & 0 & 0\\ 0 & 0 & 0 & 0 & c_{44} & 0\\ 0 & 0 & 0 & 0 & 0 & c_{66}\end{bmatrix} \tag{7}$$

And, the elastic constant tensor in a horizontal transverse isotropic medium (HTI) can be described as,

$$c_{HTI} = \begin{bmatrix} c_{11} & c_{13} & c_{13} & 0 & 0 & 0\\ c_{13} & c_{11} & c_{33}-2c_{44} & 0 & 0 & 0\\ c_{13} & c_{33}-2c_{44} & c_{33} & 0 & 0 & 0\\ 0 & 0 & 0 & c_{44} & 0 & 0\\ 0 & 0 & 0 & 0 & c_{66} & 0\\ 0 & 0 & 0 & 0 & 0 & c_{66}\end{bmatrix} \tag{8}$$

Without loss of generality, take VTI case in equation (7) as an example, and based on equation (1) , the first order velocity and stress equations can be described as,

$$\begin{aligned}
\frac{\partial\sigma_{xx}}{\partial x} + \frac{\partial\sigma_{xy}}{\partial y} + \frac{\partial\sigma_{xz}}{\partial z} &= \rho\frac{\partial V_x}{\partial t}\\
\frac{\partial\sigma_{yx}}{\partial x} + \frac{\partial\sigma_{yy}}{\partial y} + \frac{\partial\sigma_{yz}}{\partial z} &= \rho\frac{\partial V_y}{\partial t}\\
\frac{\partial\sigma_{zx}}{\partial x} + \frac{\partial\sigma_{zy}}{\partial y} + \frac{\partial\sigma_{zz}}{\partial z} &= \rho\frac{\partial V_z}{\partial t}
\end{aligned} \tag{9}$$

and,

$$\begin{aligned}
\frac{\partial \sigma_{xx}}{\partial t} &= c_{11}\frac{\partial V_x}{\partial x} + (c_{11} - 2c_{66})\frac{\partial V_y}{\partial y} + c_{13}\frac{\partial V_z}{\partial z} \\
\frac{\partial \sigma_{yy}}{\partial t} &= (c_{11} - 2c_{66})\frac{\partial V_x}{\partial x} + c_{11}\frac{\partial V_y}{\partial y} + c_{13}\frac{\partial V_z}{\partial z} \\
\frac{\partial \sigma_{zz}}{\partial t} &= c_{13}\frac{\partial V_x}{\partial x} + c_{13}\frac{\partial V_y}{\partial y} + c_{33}\frac{\partial V_z}{\partial z} \\
\frac{\partial \sigma_{yz}}{\partial t} &= c_{44}(\frac{\partial V_y}{\partial z} + \frac{\partial V_z}{\partial y}) \\
\frac{\partial \sigma_{xz}}{\partial t} &= c_{44}(\frac{\partial V_x}{\partial z} + \frac{\partial V_z}{\partial x}) \\
\frac{\partial \sigma_{xy}}{\partial t} &= c_{66}(\frac{\partial V_x}{\partial y} + \frac{\partial V_y}{\partial x})
\end{aligned} \tag{10}$$

where $(V_x, V_y, V_z)$ is the velocity vector.

**Staggered-grid finite difference approximation**

For simplicity, let's consider a univariate function $f(x)$, then the $2N^{th}$ staggered-grid FD formulation is,

$$\delta_{2N} f = \frac{1}{\Delta x}\sum_{m=0}^{N-1} a_m[f(x + \frac{2m+1}{2}\Delta x) - f(x - \frac{2m-1}{2}\Delta x)] \tag{11}$$

where, $a_m$ is the coefficient of the fourth-order FD approximation to the first-order derivative. Now consider a 3-D grid in Cartesian coordinates $(l_x\Delta x, l_y\Delta y, l_z\Delta z)$ at time $n\Delta t$, where $\Delta x, \Delta y, \Delta z$ are the grid size in X, Y and Z directions and $\Delta t$ is time step. Figure 1 shows the schematic of staggered-grid discretization for different parameters. The shear stress component, take $\sigma^n_{xy}$ as an example, is sampled as $\sigma^n_{xy}(l_x + \frac{1}{2}, l_y + \frac{1}{2}, l_z)$. The velocity component, take $V_x$ as an example, is sampled as $V_x^{n+\frac{1}{2}}(l_x + \frac{1}{2}, l_y + \frac{1}{2}, l_z)$ , where n denotes time. Therefore, equation (9) can be discretized as,

$$\begin{aligned}
V_x^{n+\frac{1}{2}} &= V_x^{n-\frac{1}{2}} + \tfrac{\Delta t}{\rho}(\delta_x\sigma^n_{xx} + \delta_y\sigma^n_{xy} + \delta_z\sigma^n_{xz}) \\
V_y^{n+\frac{1}{2}} &= V_y^{n-\frac{1}{2}} + \tfrac{\Delta t}{\rho}(\delta_x\sigma^n_{xy} + \delta_y\sigma^n_{yy} + \delta_z\sigma^n_{yz}) \\
V_z^{n+\frac{1}{2}} &= V_z^{n-\frac{1}{2}} + \tfrac{\Delta t}{\rho}(\delta_x\sigma^n_{xz} + \delta_y\sigma^n_{yz} + \delta_z\sigma^n_{zz})
\end{aligned} \tag{12}$$

and, we take $\delta_x\sigma^n_{xx}$ as an example,

$$\delta_x\sigma^n_{xx}(l_x + \frac{1}{2}, l_y, l_z) = \frac{1}{\Delta x}\sum_{m=0}^{N-1} a_m[\sigma^n_{xx}(l_x + m + 1, l_y, l_z) - \sigma^n_{xx}(l_x + m, l_y, l_z)] \tag{13}$$

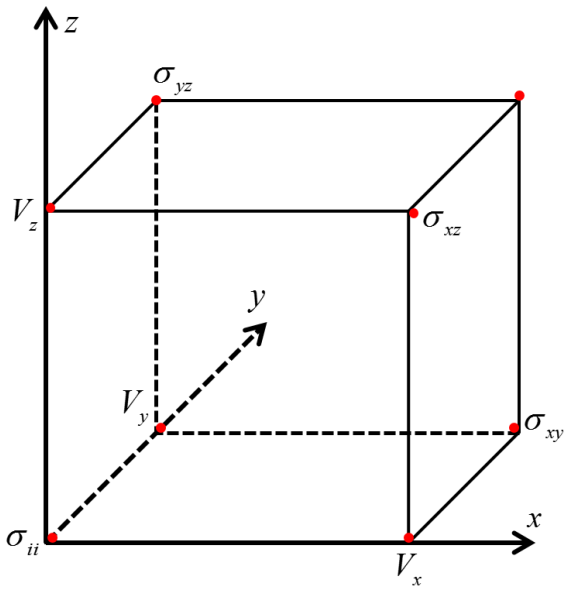


FIG. 1. Schematic of staggered-grid discretization for different parameters.

Likewise, equation (10) can be discretized as,

$$\begin{aligned}
\sigma_{xx}^{n+1} &= \sigma_{xx}^{n} + \Delta t[c_{11}\delta_x V_x^{n+1/2} + (c_{11} - 2c_{66})\delta_y V_y^{n+1/2} + c_{13}\delta_z V_z^{n+1/2}] \\
\sigma_{yy}^{n+1} &= \sigma_{yy}^{n} + \Delta t[(c_{11} - 2c_{66})\delta_x V_x^{n+1/2} + c_{11}\delta_y V_y^{n+1/2} + c_{13}\delta_z V_z^{n+1/2}] \\
\sigma_{zz}^{n+1} &= \sigma_{zz}^{n} + \Delta t[c_{13}\delta_x V_x^{n+1/2} + c_{13}\delta_y V_y^{n+1/2} + c_{33}\delta_z V_z^{n+1/2}] \\
\sigma_{yz}^{n+1} &= \sigma_{yz}^{n} + \Delta t c_{44}[\delta_y V_z^{n+1/2} + \delta_z V_y^{n+1/2}] \\
\sigma_{xz}^{n+1} &= \sigma_{xz}^{n} + \Delta t c_{44}[\delta_x V_z^{n+1/2} + \delta_z V_x^{n+1/2}] \\
\sigma_{xy}^{n+1} &= \sigma_{xy}^{n} + \Delta t c_{66}[\delta_x V_y^{n+1/2} + \delta_y V_x^{n+1/2}]
\end{aligned} \tag{14}$$

## The hybrid perfectly matched layer

As a simulation is performed at local, regional scale, energy at artificial boundaries should be absorbed. During last decades, scholars have proposed a variety of methods for this purpose. The perfectly matched layer (PML) is first proposed by Berenger (1994) based on Maxwell's equations. This method has been proven to be much more efficient compared with previously developed absorbing methods (Collino and Tsogka, 2001; Komatitsch and Tromp, 2003; Festa and Vilotte, 2005). As can be seen in Figure 2, the main idea of PML is to split velocity and stress fields into two parts (Chew and Weedon, 1994; Collino and Monk, 1998; Collino and Tsogka, 2001) and add a damping profile $d_x(x)$ ($d_x(x)$ equals to 0 in the physical domain whereas is greater than 0 when in PML layer (take x direction as an example)) into the splitting wave equation so as to suppress the arti-

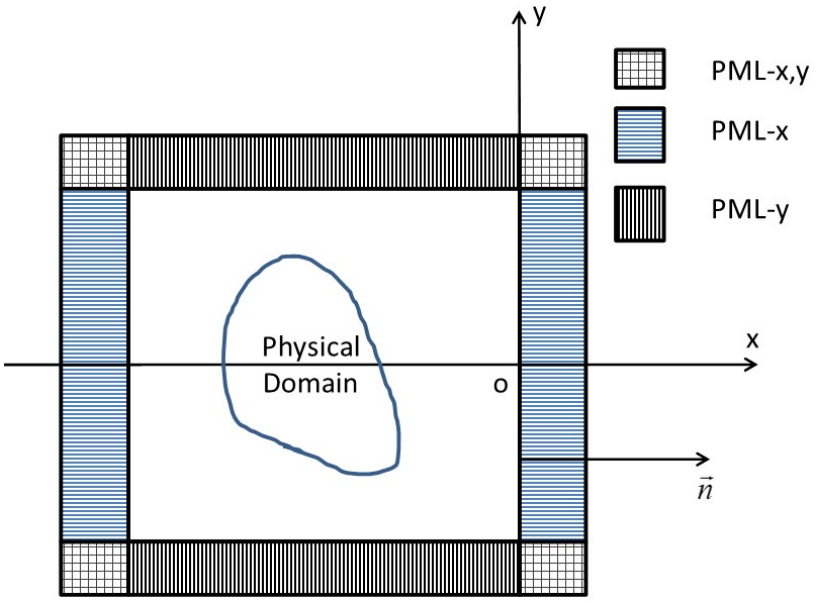


FIG. 2. PML layers outside the physical domain.

ficial reflections coming from the boundaries. Therefore, a new operator $\nabla_{\tilde{x}} = [\frac{\partial}{\partial \tilde{x}}, \frac{\partial}{\partial y}, \frac{\partial}{\partial z}]$ can be derived, where $\frac{\partial}{\partial \tilde{x}} = \frac{1}{s_x}\frac{\partial}{\partial x}$, $s_x = 1 + \frac{d_x}{i\omega}$. However, the split field PML has two main imperfections: 1) the velocity and stress field are required to be split into two subfields respectively; 2) its efficiency becomes poor at grazing incidence after discretization, which is because the damping coefficient is inversely proportional to the angular frequency and thus depends on the direction of propagation of the wave.

In order to improve the behavior of the discrete PML at grazing incidence, the convolutional PML(C-PML) (Kuzuoglu and Mittra, 1996) or complex frequency shifted-PML (CFS-PML) (Bérenger, 2002), which introduces a frequency-dependent term is proposed. This technique is based on the writing of PML model in the form of a convolution in time and on the introduction of memory variables so as to calculate this convolution in a recursive way. This scheme doesn't need to split the velocity-stress equation into separate terms in the FD method. The main idea of C-PML is to propose a much more general formula of compared with that in PML scheme by means of adding not only the damping profile but two other real variables and such that:

$$s_x = \kappa_x + \frac{d_x}{\alpha_x + i\omega} \tag{15}$$

And it is obvious that when $\kappa_x = 1$ and $\alpha_x = 0$, the C-PML degenerates into classic PML scheme. Figure 3 (the upper three pictures) shows snapshots of the monopole source wavefield propagation in isotropic media with C-PML absorbing layers. The boundary artificial reflections are effectively suppressed at different time and incidences. Easy as the C-PML is to be implemented, in some cases however, compared with the split PML scheme, it suffers some degree of instability either because of its frequency-dependent term or the convolution operations. As a result, it was later found (Abarbanel et al., 2002) that C-PML for Maxwell's equations were still susceptible to manifest slowly growing spu-

rious solutions that eventually spread and pollute the physical domain. And Komatitsch and Martin (2007) observed that the C-PML encountered severe instability issues in elastic anisotropic media. Figure 3 (the lower three pictures) shows snapshots of the monopole source wavefield propagation in VTI media with C-PML absorbing layers. As we can see when the wavefield is traveling at above 1.2 ms, a bunch of artificial reflections emerge at the edges of the snapshots. The multiaxial perfectly matched layer, known as M-PML, which is believed to be very stable for even extremely anisotropic media, is therefore developed (Meza-Fajardo and Papageorgiou, 2008). Differing from equation (15), $s_x$ in M-PML is,

$$s_x = \kappa_x + \frac{d_x + m_{x/z} d_z}{i\omega} \tag{16}$$

where $m_{x/z}$ is a weighting factor. Figure 4 (the upper three pictures) shows snapshots of the monopole source wavefield propagation in isotropic media with M-PML absorbing layers. Most of the boundary artificial reflections are effectively suppressed. However, compared with Figure 3 (the upper three pictures), there are still feeble boundary reflections in some incidences. However, Figure 4 (the lower three pictures) shows snapshots of the monopole source wavefield propagation in VTI media with M-PML absorbing layers. Compared with Figure 3 (the lower three pictures), the M-PML in anisotropic media reveals a better performance, though some minor artificial reflections still exist in some incidences, which can be reduced with increasing PML layers at a price of higher computational cost.

To achieve both accuracy and stability in the modeling, we introduce a hybrid PML that integrates the advantages of both the C-PML and the M-PML through the optimization of the damping profile. Because the C- PML and M-PML are independent on each other, we can combine the two to form a hybrid one as

$$s_x = \kappa_x + \frac{d_x + m_{x/z} d_z}{\alpha_x + i\omega} \tag{17}$$

In order to transform the above equation to the time domain, convolution or auxiliary variables are required. This procedure can be completed easily by an integration of the C-PML and the M-PML. Compared to the traditional PML and the C-PML, though the optimized $\alpha_x$ and $\kappa_x$ can greatly improve the absorbing efficiency without losing accuracy, it is still not stable enough in the modeling of TTI media. We therefore let m, the M-PML parameter, be optimized between 0.005 and 0.02. In this way, we achieve absolute stability while losing little accuracy. Figure 4 shows snapshots of a monopole source wavefield propagation in both isotropic and anisotropic medium with hybrid-PML absorbing layers. The boundary artificial reflections are effectively suppressed at different time and incidences for both isotropic and anisotropic medium.

Since we have discussed the staggered-grid finite difference method and the absorbing layer in 3D medium, Figure 6 shows the wavefield propagation in an isotropic 3D medium, the parameters of the model are shown in Table 1. As can be seen in Figure 6 from (a) to (d) the wavefield propagates from the borehole to the outside formation, when encountering the interface in (c), a part of the energy transmit into the second layer and the other part of it's energy reflects back.

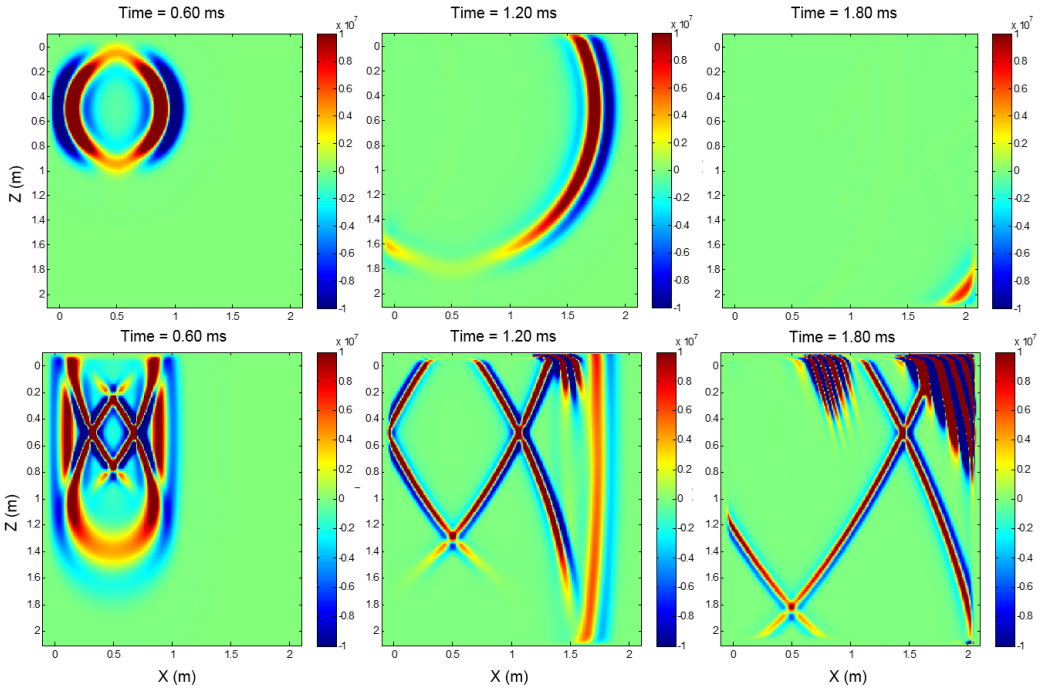


FIG. 3. Snapshots of the monopole source wavefield propagation in both isotropic media (upper three) and inosotropic meida (lower three) with C-PML absorbing layers.

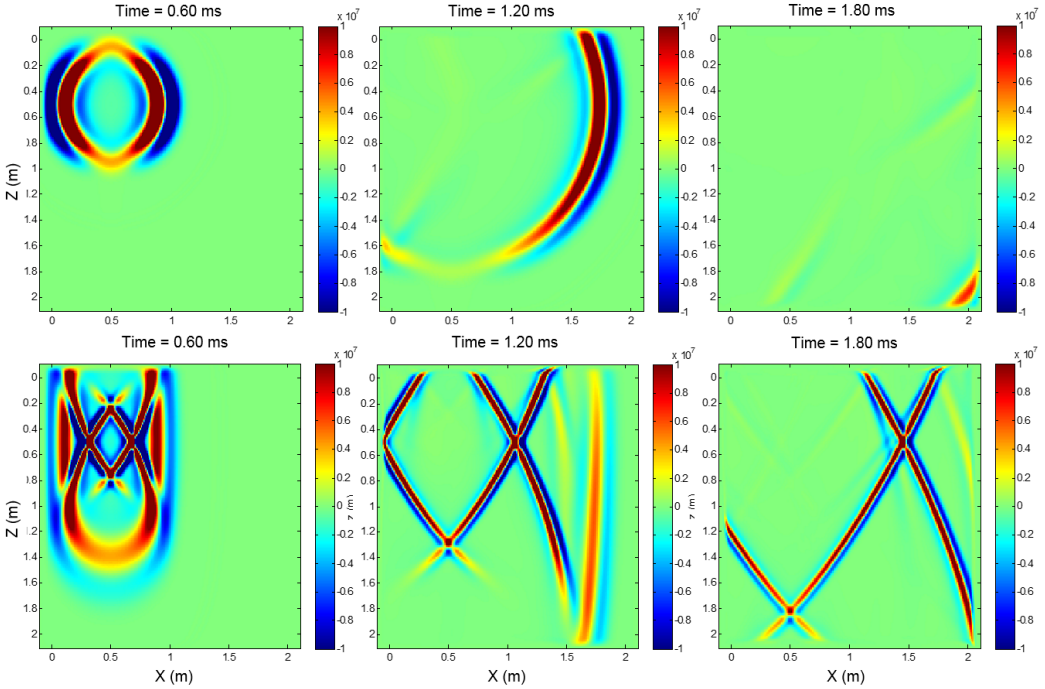


FIG. 4. Snapshots of the monopole source wavefield propagation in both isotropic media (upper three) and inosotropic meida (lower three) with M-PML absorbing layers.

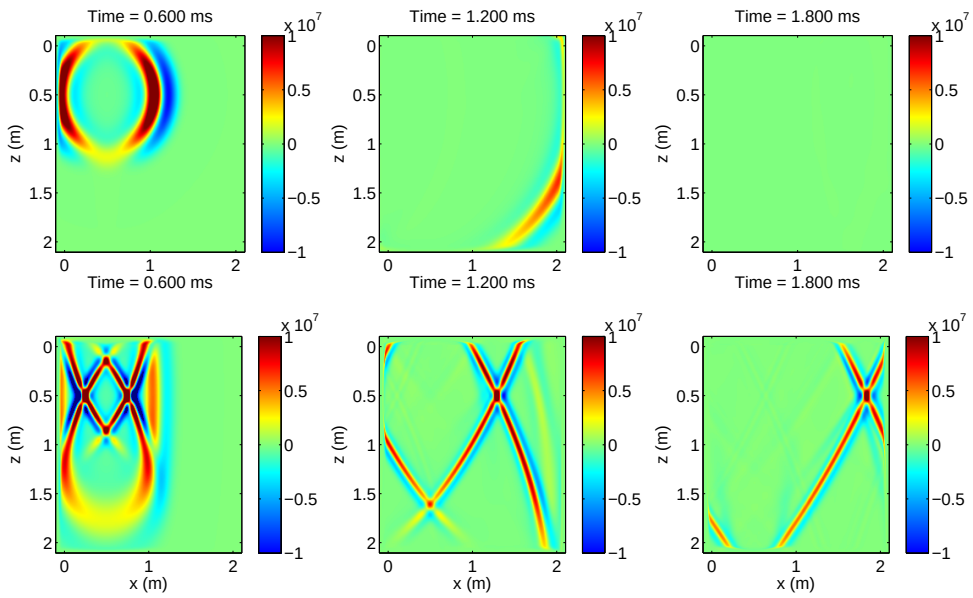


FIG. 5. Snapshots of the monopole source wavefield propagation in both isotropic media (upper three) and inosotropic meida (lower three) with H-PML absorbing layers.

## Numerical simulation for dipole source

For wavefield propagation with a monopole source, when it propagates in slow formation (S wave velocity in the formation is smaller than the acoustic wave velocity in the borehole), the receivers in the borehole cann't receive the S wave signals. This flaw urges the development of dipole or even multipole acoustic well logging. Dipole transmitters are effectively pistons that create a pressure increase on one side of the borehole and a decrease on the other (Close et al., 2009).

Table 1. The parameters for 3D modeling of wavefield propogation.

| | $V_{f(m/s)}$ | $V_{P(m/s)}$ | $V_{S(m/s)}$ | $\rho_{(k/cm^3)}$ |
|---|---|---|---|---|
| Borehole | 1500 | - | - | 1.0 |
| Near Borehole formation | - | 3000 | 1200 | 2.5 |
| Second layer | - | 4000 | 2300 | 2.5 |

For sonic waveforms with a dipole source, the wavefield inside the borehole and in the formation outside the borehole are

$$\begin{aligned} \mathbf{u} &= \nabla\varphi_f \\ \mathbf{u} &= \nabla\varphi + \nabla \times \Psi \end{aligned} \tag{18}$$

where vector $\mathbf{u}$ is the wavefield displacement, $\varphi_f$ denotes its potential in borehole fluid, $\varphi$ is the compressional wave potential in formation, shear wvae potential $\Psi$ can be described as,

$$\Psi = \chi\widehat{\mathbf{z}} + \nabla \times (\eta\widehat{\mathbf{z}}); \tag{19}$$

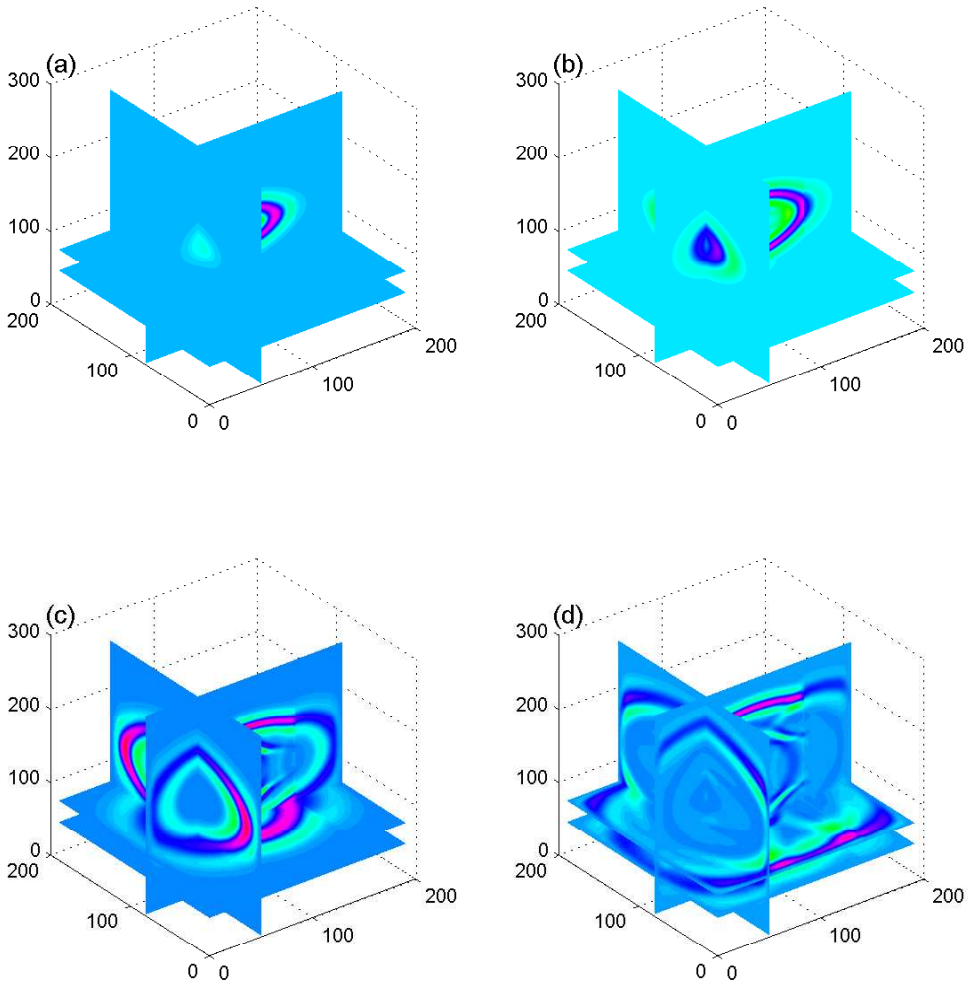


FIG. 6. Snaopshots of wave propagation in 3D medium.

where $\chi$ and $\eta$ are the SH- and SV- wave displacement potential, respectively, which satisfy the wave equation with a shear wave velocity. They can be described (Tang and Patterson, 2009) as,

$$\begin{aligned} \chi(\omega; r, z) &= \frac{S(\omega)\cos(\phi)}{4\pi} \int_{-\infty}^{+\infty} D(\omega, k) K_1(sr) e^{ikz} dk \\ \eta(\omega; r, z) &= \frac{S(\omega)\sin(\phi)}{4\pi} \int_{-\infty}^{+\infty} F(\omega, k) K_1(sr) e^{ikz} dk \end{aligned} \tag{20}$$

where $S(\omega)$ is the source spectrum; $\phi$ is the angle between the direction of particle polarization of the wave and the source orientation; $D(\omega, k)$ and $F(\omega, k)$ are undetermined functions dependent on the boundary conditions; $K_1(sr)$ is modified Bessel function with s of radial wave number.

The far field solution for the SH- and SV-wave displacement components can then be described (Tang et al., 2014) as,

$$\begin{aligned} u_\phi &\sim [i\rho\beta\omega D(\omega, k_0)\sin\theta\cos\phi]\frac{e^{i\omega R/\beta}}{4\pi\mu R}S(\omega) \\ u_\theta &\sim [\rho\omega^2 F(\omega, k_0)\sin\theta\sin\phi]\frac{e^{i\omega R/\beta}}{4\pi\mu R}S(\omega) \end{aligned} \tag{21}$$

where $\rho$ and $\mu$ are formation density and shear modulus.

The received waveforms recorded by the receivers are affected by multiple effects including the source radiation from borehole to formation, transmitted wave reflection derived from the reflectors in the formation and responses of the borehole to the reflected waves, as well as the wavefield amplitude attenuation during wave propagation along the wave path, which can be described as a convolution model in frequency domain (Tang and Patterson, 2009),

$$RWV(\omega) = S(\omega) * RD(\omega) * RF(\omega) * RC(\omega)\frac{e^{i\omega D/\beta}}{D}e^{-\frac{\omega D}{2Q_\beta \beta}} \tag{22}$$

in which RWV denotes the received reflections; $S(\omega)$ is the source spectrum; $RD(\omega)$ stands for the borehole radiation (Meredith, 1990); $RC(\omega)$ is related to borehole reception response (Peng et al., 1993); and $RF(\omega)$ is the acoustic reflectivity at the reflector. D is the total distance of a wave traveling from a source to the receiver; $Q_\beta$ denotes the shear wave attenuation. According to Tang (Tang et al., 2014) , the far-field radiation for $SH-$ and $SV-$ waves ($RD_{SH}$ and $RD_{SV}$) can be described as

$$\begin{aligned} RD_{SH} &= i\rho\beta\omega D(\omega, k_0)\sin\theta\cos\phi, \\ RD_{SV} &= \rho\beta\omega F(\omega, k_0)\sin\theta\sin\phi, \end{aligned} \tag{23}$$

According to elastic reciprocity (Achenbach, 2003), Tang (Tang et al., 2014) points out that the radiation and reception patterns both for SH- and SV- waves are equal,

$$RC(\omega, \theta) = RD(\omega, \theta); \tag{24}$$

For simplicity, the wave field attenuation factor $e^{-\frac{\omega D}{2Q_\beta \beta}}$ in equation (22) will not be discussed here and only the SH component will be discussed in the following section. The SH reflection coefficient in isotropic meidium is,

$$R_{(SH)} = \frac{\rho_1\beta_1\cos\varphi_1 - \rho_2\beta_2\cos\varphi_2}{\rho_1\beta_1\cos\varphi_1 + \rho_2\beta_2\cos\varphi_2} \tag{25}$$

In combination of equations from equation (23) to equation (25), the received SH reflection signal according to equation (22), $RWV_{SH}(\omega)$ is

$$RWV_{SH}(\omega) = S(\omega) * RD_{SH} * R_{(SH)} * RD_{SH}\frac{e^{i\omega D/\beta}}{D} \tag{26}$$

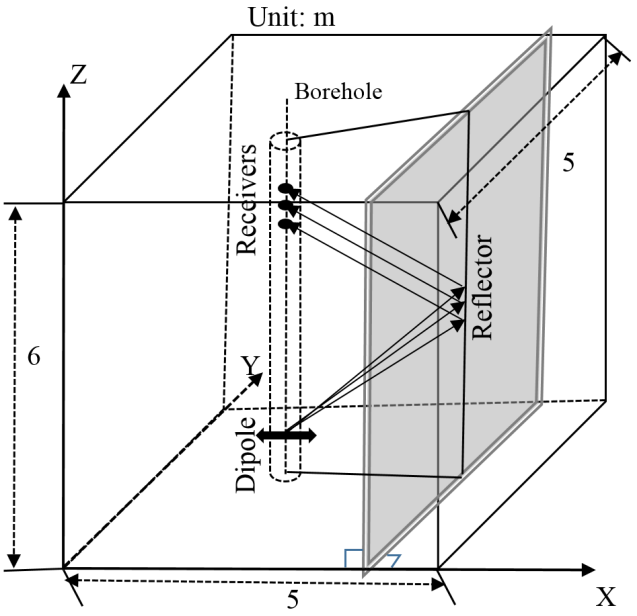


FIG. 7. The 3D profile of the isotropic model with dipole source and quadrupole receivers.

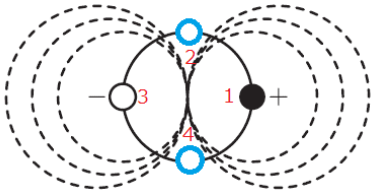


FIG. 8. Displacement of receivers around tool.

Based on the low frequency used in dipole acoustic logging, wider lateral detection depth is available. In this discussion, simulation of dipole acoustic wave propagation is conducted in isotropic media. As we can see in Figure 7, a dipole source is oriented along the x-axis of the coordinate system on the tool and makes an angle of $\phi$, where $\phi$ changes from 0 degree to 90 degrees with each change of 15 degrees. The reflector, being 3 m away from the borehole, is parallel to the borehole, which means the dip angle $\theta$ in equation (21) equals to $90°$.

The borehole is water filled with a diameter of the borehole of 0.21 m. The dipole source is located in the fluid-filled borehole. The distance of the first receiver to the source is 0.15 m, with altogether 30 receiver stations along the axis of the tool whose spacing from each other is 0.15 m. And each receiver station is populated by four azimuthal receivers evenly spaced around the tool. As a matter of simplicity, we denote the two sub-receivers parallel to the dipole source as receiver 1 and 3 and denote the other two which are perpendicular to the dipole source as receiver 2 and receiver 4, as can be seen in Figure 8. The dominant frequency is 3 kHz.

Therefore, when the source orientation is along the reflector strike, according to equation (21), a pure SH wave and its corresponding SH reflection are generated, shown in Figure 9. Figure 9 (a) shows the received reflections of receiver 1 (red) and receiver 3 (blue). Because of the radiation direction, SH signals received by receiver 1 and receiver 3 are supposed to have a phase difference resulting from different arrival time of SH reflections to receiver 1 and receiver 3, which coincides with Figure 9 (a). Theoretically, the energy received by receivers 2 and 4 will be canceled out due to the property of the dipole source, which is proved by Figure 9 (b).

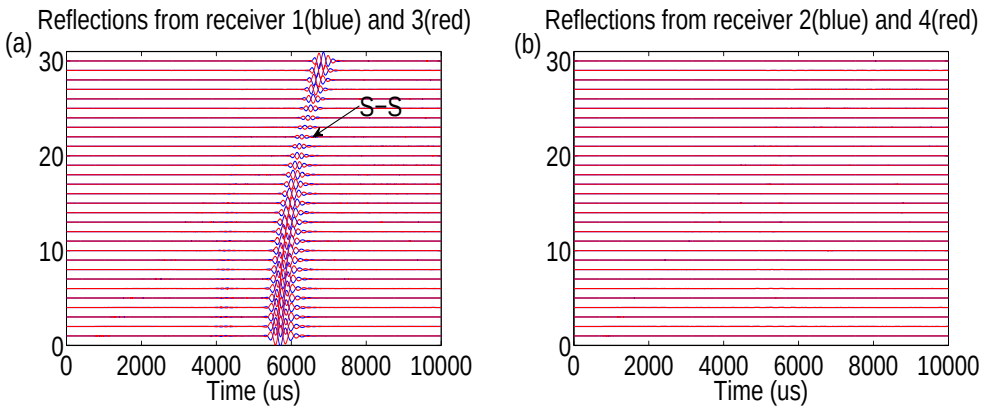


FIG. 9. (a) Received reflections of receiver 1 (red) and receiver 3 (blue); and (b) Received reflections of receiver 1 (red) and receiver 3 (blue).

For situations when $90° > \phi > 0°$ , the reflection SH, SV and P are supposed to be received by the four receivers around the tool. Figure 10 shows the results when $\phi$ is $30°$ and $60°$. Take Figure 10 (a) as an example, the reflections recorded by receiver 1 and 3 are leaky P wave reflection, leaky P-SV reflection and S-S reflection. When dominant frequency increases, the leaky P wave will be triggered by a dipole source (Tang and Cheng, 2004). Apparently, the P-P and P-SV reflections received by receiver 1 and 3 or by receiver 2 and 4 are identical in Figure 10. Whereas, for the S-S reflections, for both receiver pairs 1-3 and 2-4, the reflection signals show a distinctive phase difference when the offsets are relatively small. With the increasing of the offset, they begin to merge with each other. This means the recorded signals are dominant by SH wave when the offset is small, and the SV wave plays a dominant role when the receiver is comparatively further away from the source. Compared with the received reflections when $\phi = 30°$ (Figure 10 (a) and (b)), when $\phi$ increases, the S-S reflections begin to merge at a closer offset, that is, the SH reflection changes into SV reflections with the increase of $\phi$.

When the reflector azimuth is perpendicular to the orientation of the dipole source ( $\phi$ is $90°$), a pure SV wave and its corresponding SV reflection are generated, shown in Figure 11. Figure 11 (a) shows the received reflections of receiver 1 (red) and receiver 3(blue). The reflections recorded by receiver 1 and 3 are leaky P wave reflection, P-SV reflection and pure SV-SV reflection. Figure 11 (b) shows the received reflections of receiver 2 (red) and receiver 4 (blue), which shows a perfect match of both received signals compared with those of receiver 1 and 3. This is because receiver 2 and 4 have the same distance with the reflector.

It is not difficult to find out from the above results that the P-P reflected wave amplitude as well as the P-SV wave amplitudes vary with the azimuth angle of the reflector: the amplitudes increase with the azimuth angle of the reflector. Whereas, the P-SV wave amplitude variation trend versus the offset from near to far is opposite to that of the P-P wave. For the S-S reflection, more detailed analysis will be presented in the following discussion.

Figure 12 shows the received full wave signals of receiver 1 from $\phi = 0°$ to $\phi = 90°$ with an offset ranging from of 1.5 m to 3.75 m. From Figure 12, when the offset is 1.5

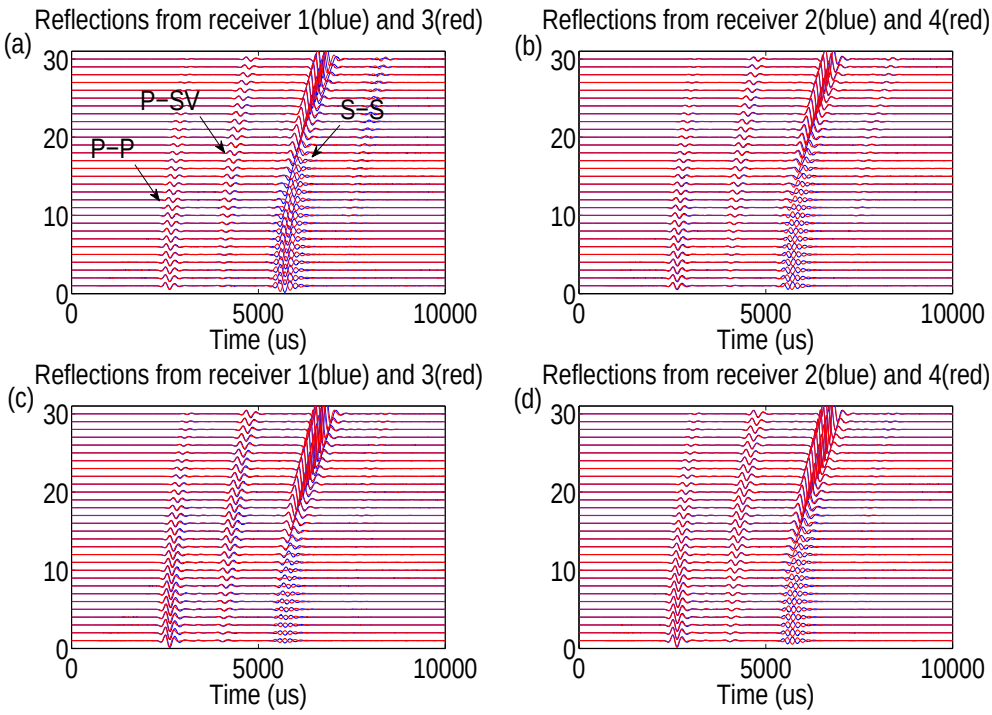


FIG. 10. (a) and (b) Received reflections when $\phi$ is $30°$; (b) and (d) Received reflections when $\phi$ is $60°$ .

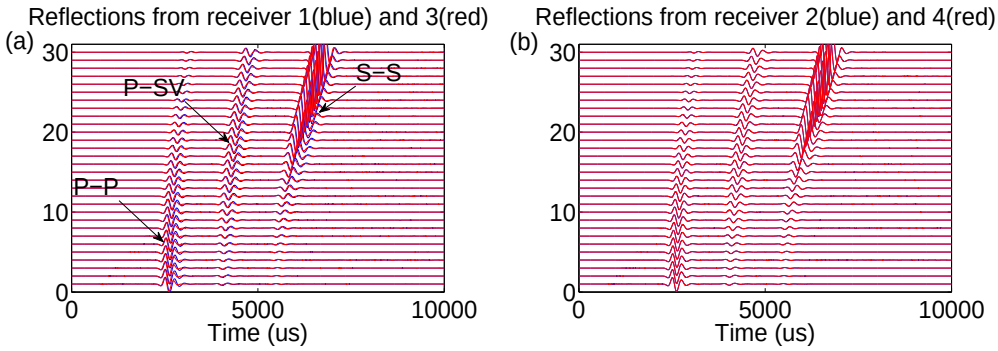


FIG. 11. (a) Received reflections of receiver 1 (red) and receiver 3 (blue); (b) and (d) Received reflections of receiver 2 (red) and receiver 4 (blue) .

m, we can see P- and S- head wave, P-P reflection, P-SV converted wave and the S-S wave respectively. With the increase of an azimuth angle between the source and reflector, the SV wave energy increases while the SH wave energy decreases due to the relationship between the source to reflector angle and the S wave polarization in equation (23), shown in the rectangle area in Figure 12. Results received by receiver 3 show quite similar property, which we won't present here.

Figure 13 shows the correspondent extracted normalized reflection signals of receiver 1 from $\phi = 0°$ to $\phi = 90°$ with an offset ranging from of 1.5 m to 3.75 m. It is clear that the P-P reflection amplitude (in the dashed red rectangle) increases with the azimuth angle

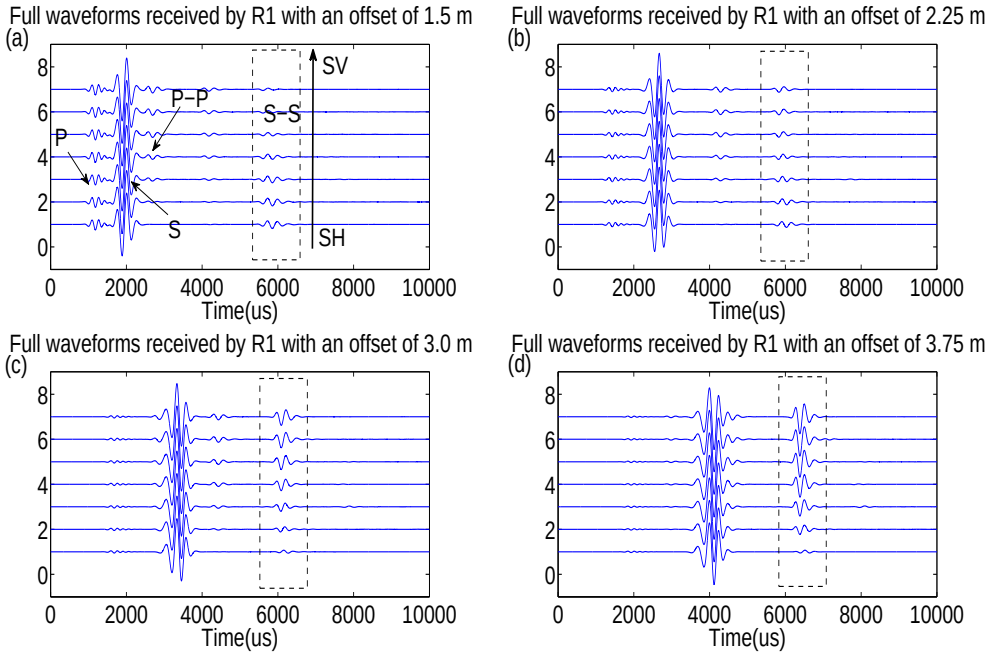


FIG. 12. Full waveforms of R1 with an offset of (a) 1.5 m, (b) 2.25 m, (c) 3.0 m and (d) 3.75 m.

of the reflector while decreases with the offset being from near to far. Whereas for the S-S reflection signals in the dashed black rectangle , because of the transformation between SH- to SV- wave signals, there's no such trend in terms of the azimuth angle and the offset, which differs from the result from (Wei and Tang, 2012). This is because not only is the amplitude of S-S reflection related to the azimuth angle, but also it is related to the offset from the source to the receiver.

Figure 14 shows received full wave signals of receiver 2 from $\phi = 0°$ to $\phi = 90°$ with an offset ranging from of 1.5 m to 3.75 m. It is apparent to see that from Figure 14 (a)-(d), there is no P- and S- head wave and only P-P reflection, P-SV converted wave and the S-S wave are presented, which is because the P- and S- direct waves have been canceled out regarding of the relationship of the location between the x-directional dipole source and the receiver 2 in y- direction. With the increase of an azimuth angle between the source and reflector, the SV wave energy increases, shown in the black dashed rectangle area in Figure 14. Results received by receiver 4 show quite similar property, which we won't present here. Figure 15 shows the correspondent extracted normalized reflection signals of receiver 2 from $\phi = 0°$ to $\phi = 90°$ with an offset ranging from of 1.5 m to 3.75 m. The reflected signal received by receiver 2 is the same as the full waveforms received by receiver 2. Therefore, the receivers which have an orthogonal relation with the radiation direction of a dipole source, in theory, record signal of pure reflections.

We have discussed the relationship between the offset and the S wave polarization in the above section with a variation of different azimuth angles of the reflector. In order to take a deep look into the relationship between S-S reflections amplitude and the offset, the S-S reflection from different reflector azimuth angles are extracted. Figure 16 shows the

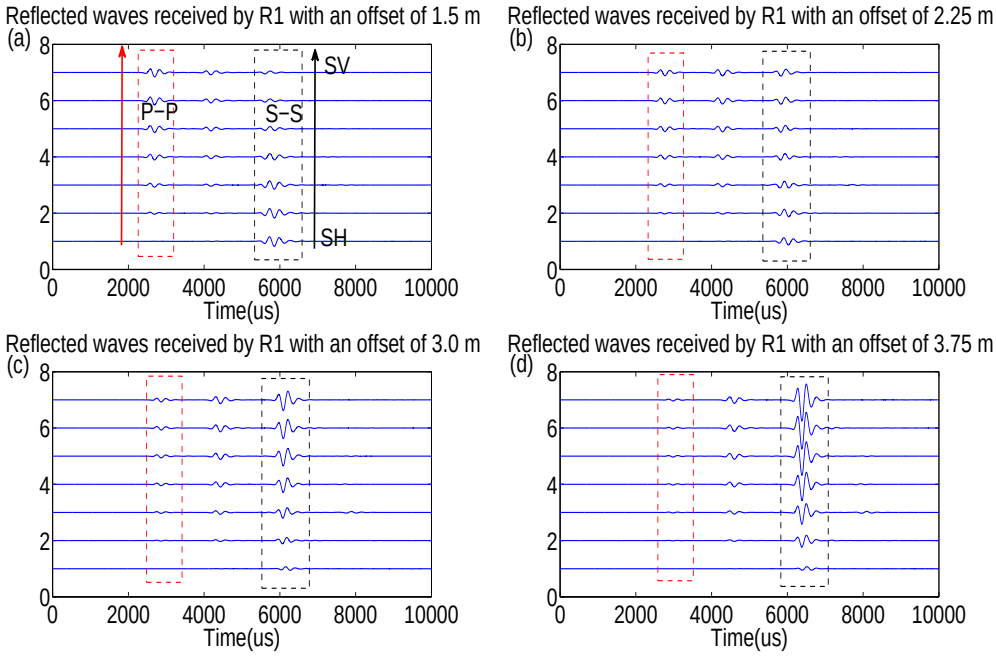


FIG. 13. (a) Reflected waves of R1 with an offset of 1.5 m; (b) Reflected waves received by R1 with an offset of 2.25 m; (c) Reflected waves received by R1 with an offset of 3.0 m; (d) Reflected waves received by R1 with an offset of 3.75 m.

normalized S-S reflected amplitude with different reflector azimuth angles versus receiver offset.

From Figure 9 to Figure 11, the SH reflection will change into SV reflection with the increase of the offset. When the azimuth angle of the reflector is small, the occurrence of this change will be in a relatively far offset (e.g. $\phi = 15°$) or even will not happen ($\phi = 0°$). It is obvious that the amplitude of SV reflection is larger than that of the SH reflection, which can be proved from Figure 16 (b), (c) and (d) where the maximum normalized S-S reflected amplitude happens to be in the far offset. And it is easy to detect that it occurs in a fixed offset (when the offset equals to 4.125 m). However, is doesn't happen in Figure 16 (a) when $\phi = 15°$. This is because the change of SH reflection to SV reflection hasn't finished and there is no pure SV reflection recorded even by the receiver with a largest offset. Now let's discuss the reason why the maximum normalized S-S reflected amplitude occurs at an offset of 4.125 m with different azimuth angles of the reflector and receivers.

Recall equation 26, let,

$$H(\omega) = S(\omega) * RD_{SH} * R_{(SH)} * RD_{SH} \tag{27}$$

According to Fourier transformation,

$$H(\omega) = \int_{-\infty}^{+\infty} h(t) e^{(i\omega t)} dt \tag{28}$$

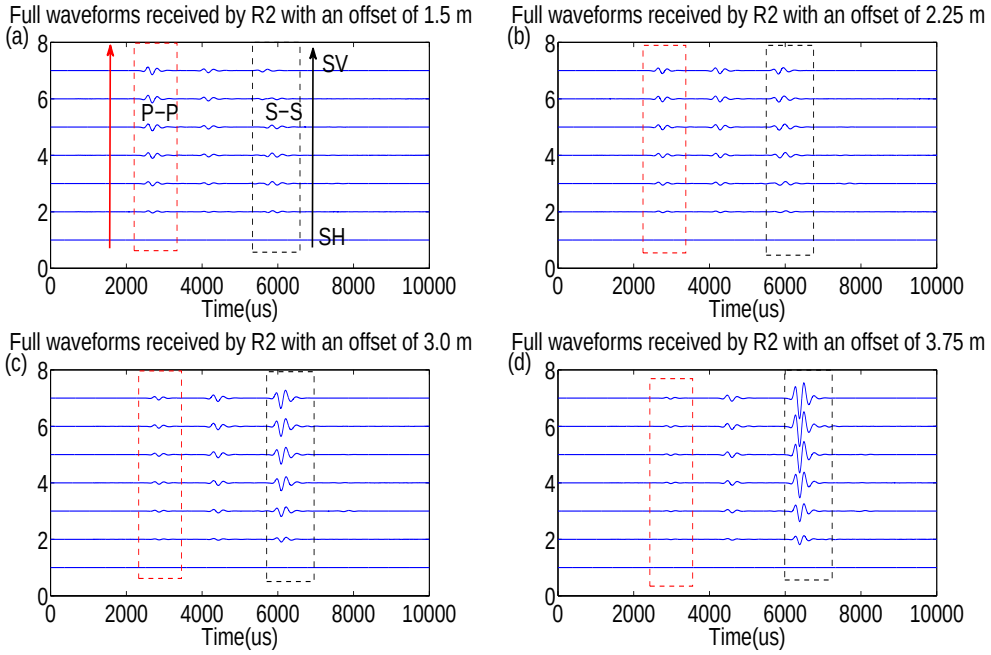


FIG. 14. (a) Full waveforms of R2 with an offset of 1.5 m; (b) Full waveforms received by R2 with an offset of 2.25 m; (c) Full waveforms received by R2 with an offset of 3.0 m; (d) Full waveforms received by R2 with an offset of 3.75 m.

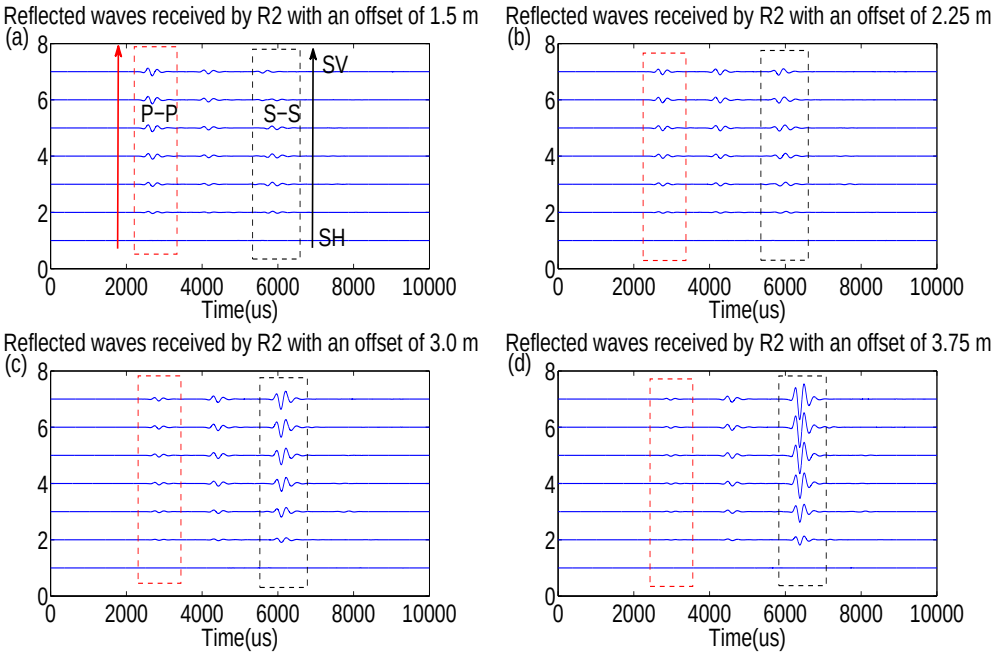


FIG. 15. (a) Reflected waves of R2 with an offset of 1.5 m; (b) Reflected waves received by R2 with an offset of 2.25 m; (c) Reflected waves received by R2 with an offset of 3.0 m; (d) Reflected waves received by R2 with an offset of 3.75 m.

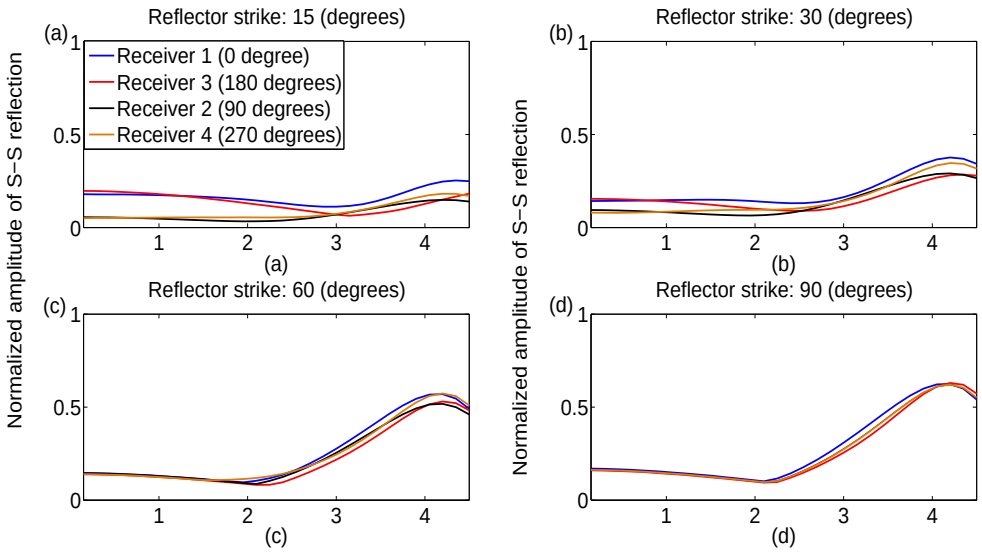


FIG. 16. Cross-plots of maximum amplitude versus receiver offset.

By multiplying $\frac{e^{i\omega D/\beta}}{D}$ into the above equation, we get

$$H(\omega)\frac{e^{i\omega D/\beta}}{D} = \frac{1}{D}\int_{-\infty}^{+\infty} h(t)e^{i\omega(t-D/\beta)}dt = RWV(\omega) \tag{29}$$

where, $h(t)$ is the Fourier transform of $H(\omega)$ in time domain and

$$h(t) = s(t)rd^2_{(SH)}r_{(SH)} \tag{30}$$

Based on equation (22), (23) and (24) , we denote the time domain form of $S(\omega)$ as $s(t)$, time domain form of $RD(\omega)$ or $RC(\omega)$ is

$$rd_{(SH)} = \frac{1}{2\pi}\int_{-\infty}^{+\infty}(i\rho\beta\omega D(\omega,k_0)\cos\phi)e^{(i\omega t)}d\omega \tag{31}$$

We get SH reflection response from equation (29) as,

$$RWV(\omega) = r_{(SH)}\frac{-\frac{1}{4\pi}\rho^2\beta^2\cos^2\phi}{D}\int_{-\infty}^{+\infty}s(t)dt\int_{-\infty}^{+\infty}\omega^2D^2(\omega,k_0)e^{iw(3t-D/\beta)}d\omega \tag{32}$$

Take the first order derivative of the above equation in terms of D and let the result equal to 0, the extrame value of this equation can be found, which is equal to determine the extreme value of,

$$f(D) = \frac{1}{D}e^{iw(3t-D/\beta)}r_{(SH)} \tag{33}$$

Combine with equation (25) and take its derivative in terms of D, we have

$$\frac{\partial f(D)}{\partial D} = \frac{\partial(\frac{1}{D}e^{iw(3t-D/\beta)}r_{(SH)})}{\partial D} = 0 \tag{34}$$

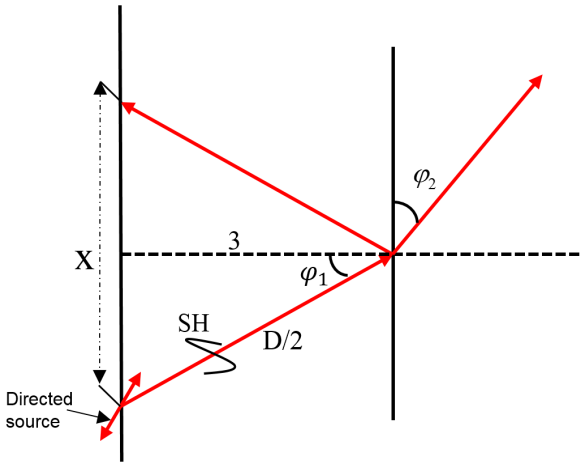


FIG. 17. S wave emission, reflection and transmission.

According to Figure 17, we have,

$$\begin{aligned} \cos\varphi_1 &= \tfrac{6}{D}; \\ \cos\varphi_2 &= \sqrt{1-\tfrac{\beta_2^2}{\beta_1^2}(1-\tfrac{36}{D^2})}; \end{aligned} \tag{35}$$

Substitute the above equation into equation (34), we find a maximum value of equation (32) when $\cos(\varphi_2) = 0$, which means the maximum value of the reflected S wave amplitude occurs when total reflection happens, which is theoretically reasonable. And we change the reflection angles from $0°$ to $60°$ with a sample rate of $0.5°$ in equation (26) to get the amplitude difference versus different reflection angles, which is shown in Figure 18. As we can see, the normalized amplitude of S wave reflection reaches to its maximum value when the reflection angle equals to $36°$. According to the model parameters, which equals to the critical angle between the two layers for S wave. And when incident angle is $36°$, the calculated offset according to Figure 17 is about 4.125 m, which equals to that with a maximum amplitude shown in Figure 16.

That's to say, based on the cross-plot of maximum amplitude versus receiver offsets, the offset with a maximum amplitude can be found and thus used to determine the total travel distance of D (see in Figure 17). Both the distance between the borehole and the reflector and the critical angle can therefore be calculated. As a result, the shear wave velocity of the second layer outside a borehole can be obtained according to Snell's law.

## DISCUSSION

The simulation for a dipole directional source is also performed in an anisotropic medium, the model that we are using is similar from Figure 7, except the size of the model is $5*5*8$ $(m^3)$. The source to the first receiver distance is 1 m and the distance between receivers is 0.16 m, with altogether 30 receivers ranging from 1 m to 5.64 m. The layer close to the borehole (the interface between the first layer and the second layer is 2 m) is a VTI medium, whose elastic parameters are,

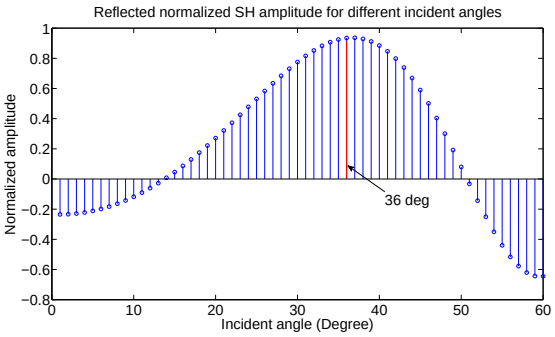


FIG. 18. Cross-plot of normalized amplitude versus different reflection angles.

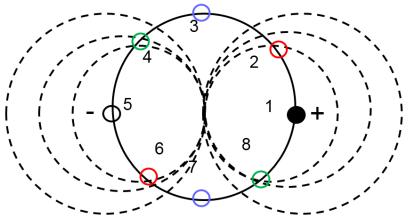


FIG. 19. Displacement of 8 receivers around tool.

$$c_{VTI} = \begin{bmatrix} 23.87 & 15.33 & 9.79 & 0 & 0 & 0 \\ 15.33 & 23.87 & 9.79 & 0 & 0 & 0 \\ 9.79 & 9.79 & 15.33 & 0 & 0 & 0 \\ 0 & 0 & 0 & 2.77 & 0 & 0 \\ 0 & 0 & 0 & 0 & 2.77 & 0 \\ 0 & 0 & 0 & 0 & 0 & 4.27 \end{bmatrix} \tag{36}$$

While the parameters in the borehole and of the second layer are identical to that of the isotropic medium, which are shown in Table 1. And for each receiver, we have 8 sub-receivers evenly spaced around the borehole, as shown in Figure 19.

Therefore, when the source orientation is along the reflector strike, the received reflections by 8 evenly spaced receivers from an offset of 1 m to 5.64 m are then shown in Figure 20, in which there is a pure SH reflection generated (from Figure 20 (a), (c) and (d)). Because of the geometrical difference of the receivers in terms of the directional dipole source and reflector, the received SH reflections by receiver pair 4 and 8 as well as by receiver pair 2 and 6 are not exactly in an opposite phase relation compared with the receiver pair 1 and 5. Receiver pair 3 and 7 can not receive reflections because of their locations in terms of the directional source.

When the angle between source orientation and the reflector strike is $30°$, the qP-P, qP-qSV reflections as well as the SH reflection are observed from each receiver, shown in Figure 21. And it is clear that the SH reflection amplitude reaches to its peak at the near offset, whereas the qSV reflection is hardly detected in the near offset, which coincides with the results that there is a transition between SH and SV reflections from the near offset to far offset. It's also worthy to notice that the amplitude of qP-qP reflection turns out to increase with the offset, which is quite the opposite compared with that in the isotropic medium.

Figure 22 and Figure 23 show the received reflections for the 8 receivers both from $\phi = 60°$ and $\phi = 90°$. With the increase of the angle between source orientation and the reflector strike, the amplitude of qP-P, qP-qSV reflections as well as the qSV-qSV reflection are increasing. However the amplitude of SH-SH reflection is decreasing and it reaches to its minimum value when $\phi = 90°$. The SH-SH reflection from different reflector azimuth

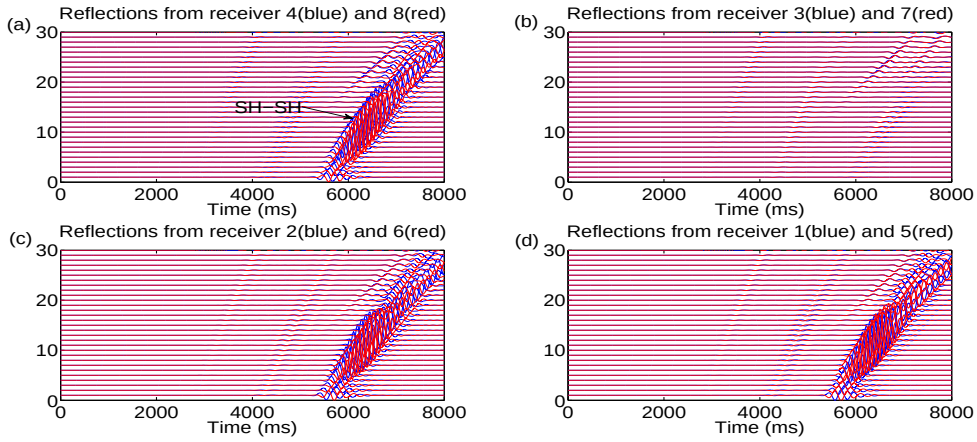


FIG. 20. Received reflections for 8 evenly spaced receivers when the strike of reflector is parallel to the radiation of the directional source.

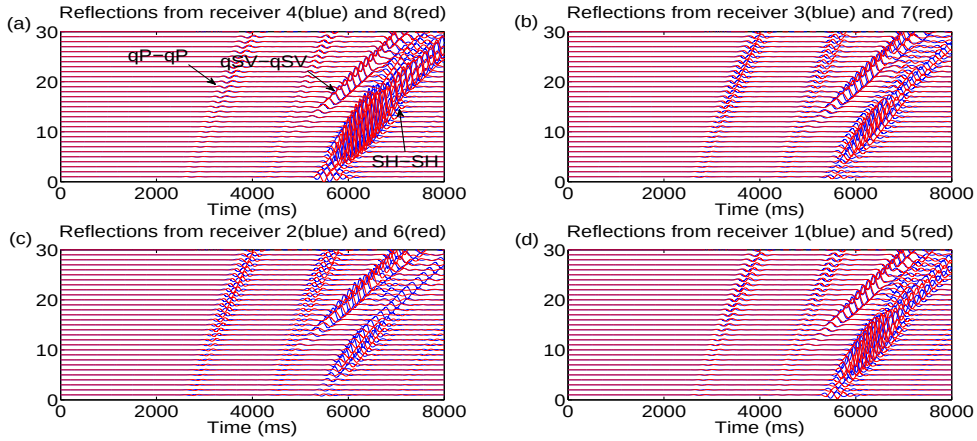


FIG. 21. Received reflections for 8 evenly spaced receivers when there is a $30^\circ$ angle difference between the strike of reflector and the radiation of the directional source.

angles is then extracted and the normalized SH-SH reflected amplitude with different reflector azimuth angles versus receiver offset are shown in Figure 24. The SH-SH amplitude of receiver 1 reaches to its peak at an offset of 2.67 m. In VTI medium, the received waveforms recorded by the receivers will be different from equation (26), the $S(\omega)$, $RC(\omega)$, $RD(\omega)$ together with the $RF(\omega)$ in equation (26) no longer be suitable for the received waveforms in VTI medium. However, in theory, the maximum value of the received SH amplitude will occur when the wave propagates to the interface with a critical angle. And from Figure 24, the relationship between the maximum amplitude and the receiver offset is not related to the azimuth angle of the reflector. In fact, the $RF(\omega)$ term plays a dominant role in the change of the SH reflection amplitude. We will introduce the SH reflection coefficient in VTI medium in the following discussion.

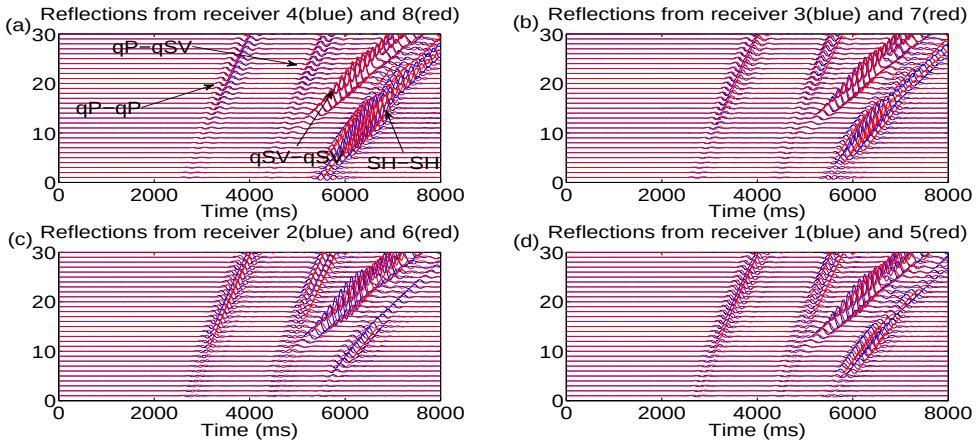


FIG. 22. Received reflections for 8 evenly spaced receivers when there is a $60^\circ$ angle difference between the strike of reflector and the radiation of the directional source.

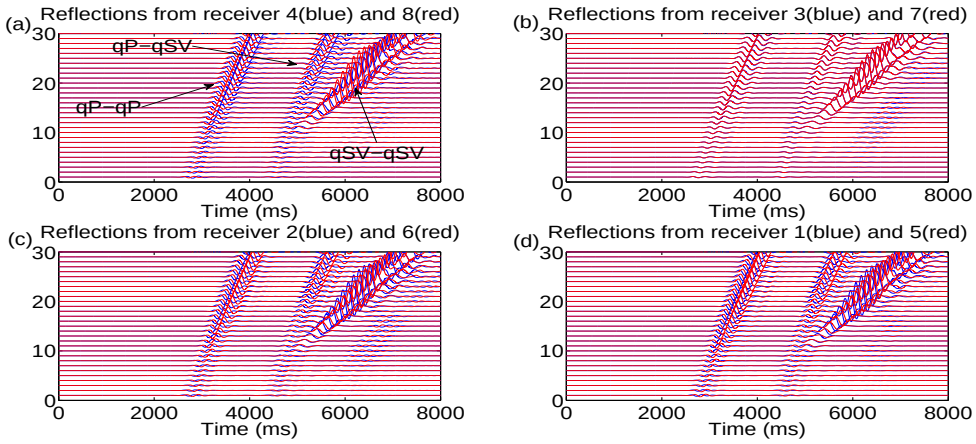


FIG. 23. Received reflections for 8 evenly spaced receivers when there is a $90^\circ$ angle difference between the strike of reflector and the radiation of the directional source.

The SH reflection coefficient $R_{SH}$, according to Slawinski (2003), can be described as,

$$R_{SH} = \frac{\frac{\sqrt{\rho_1}c_{44}^I \cos\varphi_1}{\sqrt{c_{66}^I \sin\varphi_1{}^2 + c_{44}^I \cos\varphi_1{}^2}} - \frac{\sqrt{\rho_2}c_{44}^{II} \cos\varphi_2}{\sqrt{c_{66}^{II} \sin^2\varphi_2 + c_{44}^{II} \cos^2\varphi_2}}}{\frac{\sqrt{\rho_1}c_{44}^I \cos\varphi_1}{\sqrt{c_{66}^I \sin^2\varphi_1 + c_{44}^I \cos^2\varphi_1}} + \frac{\sqrt{\rho_2}c_{44}^{II} \cos\varphi_2}{\sqrt{c_{66}^{II} \sin^2\varphi_2 + c_{44}^{II} \cos^2\varphi_2}}} \tag{37}$$

where $c_{44}^I, c_{66}^I$ and $c_{44}^{II}, c_{66}^{II}$ are the elastic constants of the incident and the refracted media; $\varphi_1, \varphi_2$ are the incident angle and transmitted angle. $\rho_1$ and $\rho_1$ denote the density of incident and transmitted layers. In this examining procedure, we wish to state the above equation in terms of incident angle only, herein, we have,

$$\frac{\sin\varphi_1}{\sqrt{\frac{c_{66}^I \sin^2\varphi_1 + c_{44}^I \cos^2\varphi_1}{\rho_1}}} = \frac{\sin\varphi_2}{\sqrt{\frac{c_{66}^{II} \sin^2\varphi_2 + c_{44}^{II} \cos^2\varphi_2}{\rho_2}}} \tag{38}$$

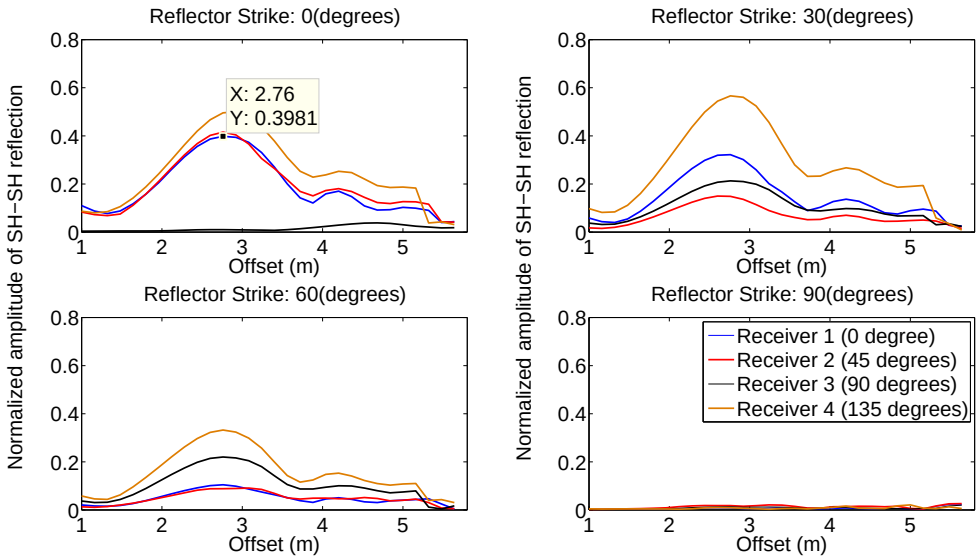


FIG. 24. Cross-plot of normalized amplitude versus different receiver offsets in VTI medium.

Solving equation (38), we have,

$$\varphi_2 = \arcsin\sqrt{\frac{\rho_1 c_{44}^{II}\sin^2_{\varphi_1}}{[\rho_2(c_{66}^{I}-c_{44}^{I})-\rho_1(c_{66}^{II}-c_{44}^{II})]\sin^2_{\varphi_1}+\rho_2 c_{44}^{I}}} \tag{39}$$

Then we change the incident angle from $0^\circ$ to $90^\circ$ with a sample rate of $0.5^\circ$ in equation (37) to get the amplitude difference versus different reflection angles, which is shown in Figure 25. As we can see, the normalized amplitude of SH reflection reaches to its maximum value when the reflection angle equals to $50.5^\circ$. And when incident angle is $50.5^\circ$, the calculated offset according to Figure 24 is about 2.76 m, which equals to that with a maximum amplitude shown in Figure 25.

## CONCLUSIONS

The 3D elastic medium staggered-grid finite difference method is discussed for the borehole acoustic wave simulation. As for the boundary artificial reflections suppression, the popular PML, C-PML and M-PML are discussed. The main idea of C-PML is to propose a much more general formula so as to improve the behavior in tackling with the grazing incidence. However, in some cases, it suffers some degree of instability either because of its frequency-dependent term or the convolution operations. The M-PML, being higher efficiency especially in grazing incidence, often suffers spurious reflections if the damping parameter is not optimized and the thickness of the PML is not large enough. A hybrid PML based on the C-PML and M-PML is proposed in this paper. The snapshots of waveforms show that the hybrid PML is well behaved in grazing incidence.

We then apply a 3D elastic staggered-grid finite difference method to the wavefield simulation for a directional dipole source with a parallel reflector rotating around it in isotropic medium. The received reflections by the four evenly spaced receivers around the

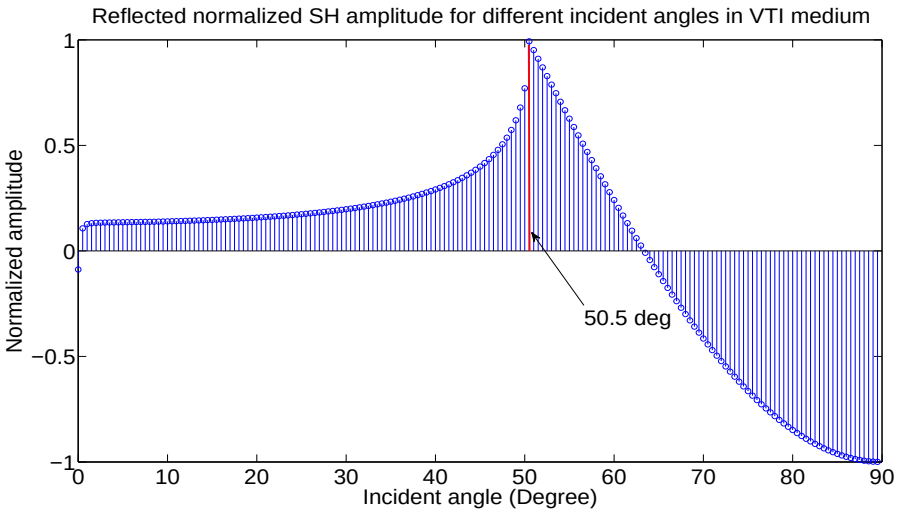


FIG. 25. Cross-plot of normalized amplitude versus different reflection angles in VTI medium.

borehole show an angular dependence on the reflector. And a transition is detected between the SH-SH reflection and SV-SV reflection with the increase of the offset. Futher analysis on the relationships between the borehole wavefield reception, radiation and reflection of S-S reflected signals show that the maximum S-S reflected amplitude occurs when the incident angle of S wave reaches to its critical value (when total reflection happens). Based on the cross-plot of maximum amplitude versus receiver offsets, the offset with a maximum amplitude can be found and thus used to determine the total travel distance of D. Both the distance between the borehole and the reflector and the critical angle can therefore be calculated. As a result, the shear wave velocity of the second layer outside a borehole can be obtained according to Snell's law.

For a further discussion, the forward simulation for a directional dipole source with a parallel reflector rotating around it in the VTI medium is also discussed. Although, the received waveforms recorded by the receivers is different from the isotropic medium. In theory, the maximum value of the received SH amplitude will occur when the wave propagates to the interface with a critical angle. The SH-SH reflection coefficient in the VTI medium is introduced and used to calculate the relationship between the incident angle and reflected amplitude. As a result, our suspicion is then approved by the simulation results of the relationship between offset and the reflected amplitude in conjunction of the calculated change of the SH-SH reflection coefficient with the incident angle.

## ACKNOWLEDGMENTS

The authors thank the sponsors of CREWES for continued support. This work was funded by CREWES industrial sponsors and NSERC (Natural Science and Engineering Research Council of Canada) through the grant CRDPJ 461179-13. Author 1 was also supported by SEG scholarship and Shell.

## REFERENCES

Abarbanel, S., Gottlieb, D., and Hesthaven, J. S., 2002, Long time behavior of the perfectly matched layer equations in computational electromagnetics: Journal of scientific Computing, **17**, No. 1-4, 405–422.

Achenbach, J. D., 2003, Reciprocity in elastodynamics: Cambridge University Press.

Alterman, Z., and Karal, F., 1968, Propagation of elastic waves in layered media by finite difference methods: Bulletin of the Seismological Society of America, **58**, No. 1, 367–398.

Berenger, J.-P., 1994, A perfectly matched layer for the absorption of electromagnetic waves: Journal of computational physics, **114**, No. 2, 185–200.

Bérenger, J.-P., 2002, Application of the cfs pml to the absorption of evanescent waves in waveguides: IEEE Microwave and Wireless Components Letters, **12**, No. 6, 218–220.

Bolshakov, A. O., Patterson, D. J., Lan, C. et al., 2011, Deep fracture imaging around the wellbore using dipole acoustic logging, *in* SPE Annual Technical Conference and Exhibition, Society of Petroleum Engineers.

Cerjan, C., Kosloff, D., Kosloff, R., and Reshef, M., 1985, A nonreflecting boundary condition for discrete acoustic and elastic wave equations: Geophysics, **50**, No. 4, 705–708.

Chew, W. C., and Weedon, W. H., 1994, A 3d perfectly matched medium from modified maxwell's equations with stretched coordinates: Microwave and optical technology letters, **7**, No. 13, 599–604.

Close, D., Cho, D., Horn, F., and Edmundson, H., 2009, The sound of sonic: A historical perspective and introduction to acoustic logging: CSEG Recorder, 34–43.

Coates, R., Kane, M., Chang, C., Esmersoy, C., Fukuhara, M., Yamamoto, H. et al., 2000, Single-well sonic imaging: High-definition reservoir cross-sections from horizontal wells, *in* SPE/CIM International Conference on Horizontal Well Technology, Society of Petroleum Engineers.

Collino, F., and Monk, P. B., 1998, Optimizing the perfectly matched layer: Computer methods in applied mechanics and engineering, **164**, No. 1, 157–171.

Collino, F., and Tsogka, C., 2001, Application of the perfectly matched absorbing layer model to the linear elastodynamic problem in anisotropic heterogeneous media: Geophysics, **66**, No. 1, 294–307.

Dong, L., She, D., Guan, L., and Ma, Z., 2005, An eigenvalue decomposition method to construct absorbing boundary conditions for acoustic and elastic wave equations: Journal of Geophysics and Engineering, **2**, No. 3, 192.

Festa, G., and Vilotte, J.-P., 2005, The newmark scheme as velocity–stress time-staggering: an efficient pml implementation for spectral element simulations of elastodynamics: Geophysical Journal International, **161**, No. 3, 789–812.

Fortin, J., Rehbinder, N., Staron, P. et al., 1991, Reflection imaging around a well with the eva full-waveform tool: The Log Analyst, **32**, No. 03.

Givoli, D., 1991, Non-reflecting boundary conditions: Journal of Computational Physics, **94**, No. 1, 1–29.

Grote, M. J., 2000, Nonreflecting boundary conditions for elastodynamic scattering: Journal of Computational Physics, **161**, No. 1, 331–353.

Guddati, M. N., and Lim, K.-W., 2006, Continued fraction absorbing boundary conditions for convex polygonal domains: International Journal for Numerical Methods in Engineering, **66**, No. 6, 949–977.

Hagstrom, T., and Hariharan, S., 1998, A formulation of asymptotic and exact boundary conditions using local operators: Applied Numerical Mathematics, **27**, No. 4, 403–416.

Hornby, B. E., 1989, Imaging of near-borehole structure using full-waveform sonic data: Geophysics, **54**, No. 6, 747–757.

Kelly, K., Ward, R., Treitel, S., and Alford, R., 1976, Synthetic seismograms: a finite-difference approach: Geophysics, **41**, No. 1, 2–27.

Komatitsch, D., and Martin, R., 2007, An unsplit convolutional perfectly matched layer improved at grazing incidence for the seismic wave equation: Geophysics, **72**, No. 5, SM155–SM167.

Komatitsch, D., and Tromp, J., 2003, A perfectly matched layer absorbing boundary condition for the second-order seismic wave equation: Geophysical Journal International, **154**, No. 1, 146–153.

Kuzuoglu, M., and Mittra, R., 1996, Frequency dependence of the constitutive parameters of causal perfectly matched anisotropic absorbers: Microwave and Guided Wave Letters, IEEE, **6**, No. 12, 447–449.

Levander, A. R., 1988, Fourth-order finite-difference p-sv seismograms: Geophysics, **53**, No. 11, 1425–1436.

Li, Y., Zhou, R., Tang, X., Jackson, J., and Patterson, D., 2002, Single-well imaging with acoustic reflection survey at mounds, oklahoma, usa, *in* 64th EAGE Conference & Exhibition.

Madariaga, R., 1976, Dynamics of an expanding circular fault: Bulletin of the Seismological Society of America, **66**, No. 3, 639–666.

Meredith, J. A., 1990, Numerical and analytical modelling of downhole seismic sources–the near and far field: Ph.D. thesis, Massachusetts Institute of Technology.

Meza-Fajardo, K. C., and Papageorgiou, A. S., 2008, A nonconvolutional, split-field, perfectly matched layer for wave propagation in isotropic and anisotropic elastic media: stability analysis: Bulletin of the Seismological Society of America, **98**, No. 4, 1811–1836.

Peng, C., Cheng, C., and Toksöz, M., 1993, Borehole effects on downhole seismic measurements: Geophysical prospecting, **41**, No. 7, 883–912.

Peng, C., and Toksöz, M. N., 1995, An optimal absorbing boundary condition for elastic wave modeling: Geophysics, **60**, No. 1, 296–301.

Slawinski, M. A., 2003, Seismic waves and rays in elastic media, vol. 34: Elsevier.

Sochacki, J., Kubichek, R., George, J., Fletcher, W., and Smithson, S., 1987, Absorbing boundary conditions and surface waves: Geophysics, **52**, No. 1, 60–71.

Tang, X., Dubinsky, V., Harrison, C. et al., 2003, Logging-while-drilling shear and compressional measurements: case histories, *in* SPWLA 44th Annual Logging Symposium Transactions.

Tang, X. M., 2004, Imaging near-borehole structure using directional acoustic-wave measurement: Geophysics, **69**, No. 6, 1378–1386.

Tang, X.-M., Cao, J.-j., and Wei, Z.-t., 2014, Shear-wave radiation, reception, and reciprocity of a borehole dipole source: With application to modeling of shear-wave reflection survey: Geophysics, **79**, No. 2, T43–T50.

Tang, X.-M., and Cheng, C. H. A., 2004, Quantitative borehole acoustic methods, vol. 24: Gulf Professional Publishing.

Tang, X.-M., and Patterson, D. J., 2009, Single-well s-wave imaging using multicomponent dipole acoustic-log data: Geophysics, **74**, No. 6, WCA211–WCA223.

Virieux, J., 1986, P-sv wave propagation in heterogeneous media: Velocity-stress finite-difference method: Geophysics, **51**, No. 4, 889–901.

Wei, Z.-T., and Tang, X.-M., 2012, Numerical simulation of radiation, reflection, and reception of elastic waves from a borehole dipole source: Geophysics, **77**, No. 6, D253–D261.

Yoon, K.-H., and McMechan, G. A., 1992, 3-d finite-difference modeling of elastic waves in borehole environments: Geophysics, **57**, No. 6, 793–804.